

Path Learning Using Different Scale Grid and Place Cells

Irmak Aykin

July 2, 2015

1 Introduction

Mammalian spatial navigation is central to most behaviors and requires an understanding of the environment at multiple spatial scales (refs in humans and rats). How these scales are established during development and how they are used when an animal forages or learns a specific spatial layout are essentially unknown. The neural substrate of spatial navigation in the rodent has been extensively studied, and several types of neurons have been found that encode specific features potentially useful for spatial navigation.

Place cells are located in the Hippocampus and have active firing fields at specific locations in 2 dimensional space, called 'place fields' (O'Keefe and Nadel, 1978). Grid cells, on the other hand, are located in the adjacent Medial Entorhinal Cortex(MEC) and they show periodic firing as a function of location. Specifically, a grid cell is activated whenever the animal traverses through any vertex of a regular grid of equilateral triangles that span the environment (Hafting et al., 2005). Both grid and place cells are organized from dorsal to ventral levels in increasing spatial field sizes. The size gradient seems to be smooth for place cells (ref), but has been shown to be modular for grid cells (ref). Place and grid cells are functionally reciprocally connected in an ordered fashion, within each level (ref).

Grid cells can be defined by three parameters: period, orientation and phase. The period of a grid cell can be defined as the spacing between the peak points of two neighboring grid fields of a given grid cell. The orientation of a grid cell is the tilt of the grid relative to a reference axis, and the phase is the displacement in the x and y directions relative to an external reference point. In other words, grid cells that belong to the same module share a common period and orientation, but their phases differ (Hafting et al., 2005).

There are plenty of place cell models in the literature, such as (Tsodyks et al., 1996), (Arleo and Gerstner, 2000), (Lengyel et al., 2003), (Lever et al., 2002) and (Bostock et al., 1991). There are also a lot of models on grid cell firing such as (Burgess et al., 2007), (Giocomo et al., 2007), (Zilli and Hasselmo, 2010) (Hasselmo et al., 2007) and (Hasselmo, 2008). However, there is only a few that discusses grid cells and place cells together. These include (Lytle et al., 2013), (Solstad et al., 2006), (McNaughton et al., 2006), (Fuhs and Touretzky, 2006) and (Savelli and Knierim, 2010). (Lytle et al., 2013) includes a computational model to construct place fields using grid fields and nonspatial inputs, and it uses dorso-ventral gradient. On the other hand,(Savelli and Knierim, 2010) addresses how an integrate-and-fire unit driven by grid-cell spike trains may transform the spatial firing pattern of grid cells into the single-peaked activity of hippocampal place cells. In their simulations the selection of grid cell inputs are accomplished by fast Hebbian plasticity alone. Similar to (Lytle et al., 2013) and (Savelli and Knierim, 2010), (Solstad et al., 2006) also constructs place fields out of appropriately weighted inputs from grid cells. The authors have found out that when the spatial phase variation in the grid cell input is high, multiple and irregularly spaced firing fields are formed. However, none of these aim to answer any questions related to development of grid cells. (McNaughton et al., 2006), on the other hand, discusses the continuous attractor network (CAN) and oscillatory interference (OI) models. It also includes a developmental model for an anatomically non-topographic MEC path integrator. In their model, Hebbian plasticity within a module generates a synaptic matrix in which neurons tuned to similar Turing layer grid phases will be strongly coupled, whereas cells with opposite phase tuning will be weakly coupled. However, there is no known anatomical difference between grid cells with different phases. Thus, coupling cells according to their phases may not have an physiological basis. Finally, (Fuhs and Touretzky, 2006) describes a symmetric, locally connected neural network that spontaneously produces a hexagonal grid of activity bumps in 2D. Nevertheless, their model is too complex such that it includes animals normalized speed, membrane voltages, symmetric and non-symmetric weight matrices and other

terms to eliminate the edge effect.

Together, grid and place cells form a topographical map for navigational tasks (Moser et al., 2008). This map can be characterized by a weight matrix, where the entries correspond to synaptic connections between grid and place cells (Burak and Fiete, 2009). In other words, if we have a network of M grid and N place cells, we can use a $(M + N) \times (M + N)$ weight matrix to keep track of all possible synaptic connections. Using a Hebbian plasticity rule with decay, these connections can be strengthened or weakened in accordance with the fields visited during behavior. Thus, a rodent learning a path through specific locations will form a weight matrix that could act as a signature for the learned path.

2 Methods

2.1 Neural Models

In our model, we consider 500 place cells with a continuously increasing field size across the ventral axis. Place fields are assumed to have Gaussian tuning curves suggested by (O’Keefe and Burgess, 1996), with the probability density function being

$$f(x, y) = \frac{\exp\left\{-\frac{1}{2(1-\rho^2)}\left[\left(\frac{x-\mu_x}{\sigma_x}\right)^2 - 2\rho\left(\frac{x-\mu_x}{\sigma_x}\right)\left(\frac{y-\mu_y}{\sigma_y}\right) + \left(\frac{y-\mu_y}{\sigma_y}\right)^2\right]\right\}}{2\pi\sigma_x\sigma_y\sqrt{1-\rho^2}} \quad (1)$$

where (μ_x, μ_y) is the mean vector and the covariance matrix is

$$\begin{pmatrix} Var(X) & Cov(X, Y) \\ Cov(X, Y) & Var(Y) \end{pmatrix} = \begin{pmatrix} \sigma_x^2 & \rho\sigma_x\sigma_y \\ \rho\sigma_x\sigma_y & \sigma_y^2 \end{pmatrix} \quad (2)$$

In the model, σ_x^2 and σ_y^2 varies from 50 to 675. σ_x^2 and σ_y^2 defines the field scale and $\rho\sigma_x\sigma_y$ defines the shape of the field. ρ is assumed to be 0, which results in circular place fields. Since the result of a Gaussian function never achieves 0, we have clipped the function and assigned the value 0 where the result of the function is less than 10^{-1} . In addition, since larger variance would result in smaller peak firing rates, to eliminate that effect, we normalize each cell with its peak firing value. The resulting place fields are shown in Figures 1(a), 1(b) and 1(c).

Grid cells, on the other hand, are assumed to consist of three 2-D cosine functions as suggested by (Solstad et al., 2006), with their gratings oriented at different angles, $\pi/3$ apart. There are also 500 grid cells with field sizes increasing continuously across the ventral axis. The gaps between grid fields increase as the grid field sizes increase, in accordance with (Brun et al., 2008) and (Hafting et al., 2005). Using (Lytle et al., 2013), we have derived the grid cell model as follows:

$$G(\mathbf{s}, \lambda, \theta, \mathbf{c}) = g\left(\sum_{k=1}^3 \cos\left(\frac{4\pi}{\sqrt{3}\lambda} \mathbf{u}(\theta_k - \theta) \cdot (\mathbf{s} - \mathbf{c})\right)\right), \quad (3)$$

where $\mathbf{s} = (x, y)$ is the location vector (1×2 vector in 2D space), k is the inter-vertex spacing between grid points (in cm), $\mathbf{c} = (x_0, y_0)$ is the spatial phase (in cm relative to the origin), $\mathbf{u}(\theta_k) = (\cos(\theta_k), \sin(\theta_k))$ is a unit vector denoting grid orientation in the direction θ_k . (\cdot denotes the inner product). In the grid cell models, we use $\theta_1 = 0$, $\theta_2 = \pi/3$ and $\theta_3 = 2\pi/3$, and the sum of 3 cosine functions are applied to $g(x)$, where $g(x) = \exp(a(x - b)) - 1$, and $a = 0.3$ and $b = -1.5$, in accordance with (de Almeida et al., 2009). We normalize each grid cell with its peak value so that the peak firing rate in each grid cell is 1. The values of λ are varied between 20 cm and 1.2 m, similar to the ones used in (Moser et al., 2014). The resulting grid fields are shown in Figures 1(d), 1(e) and 1(f).

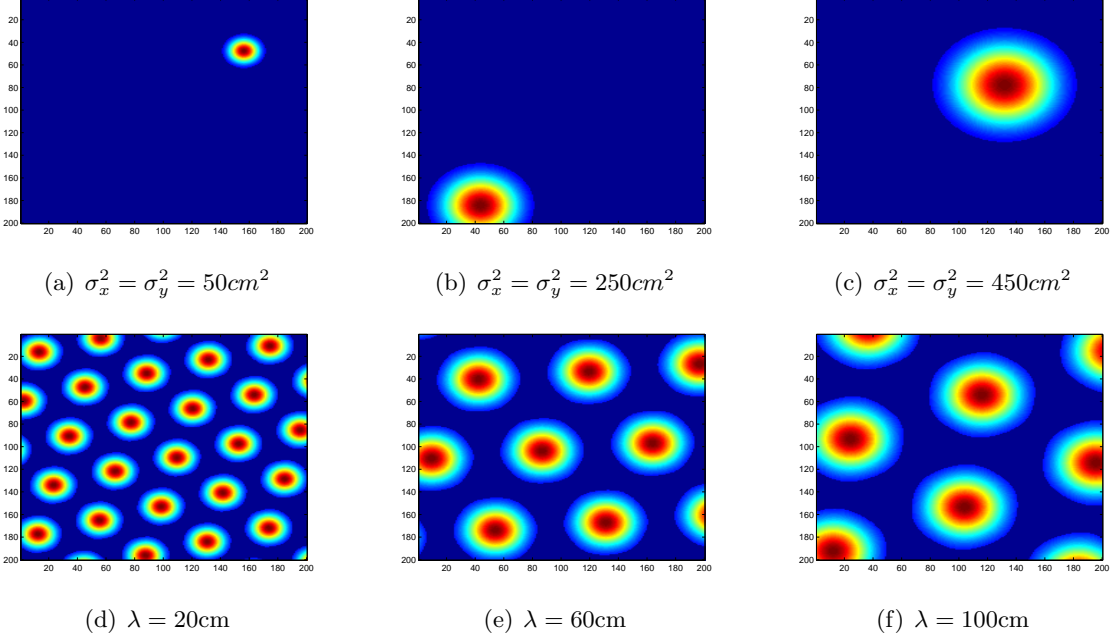


Figure 1: Place Fields with Various σ^2 Values and Grid Fields with Various λ values

2.2 Path Models

Regarding the path that the rat follows, we consider both experimental data and data obtained by simulations. The maze used for collecting experimental data is circular shaped with a radius of 1 m. Within the maze, there are several reward locations that the rat is fed when it visits those locations. Hence, once the rat learns the experiment, it does not explore the whole simulation area and tends to traverse the shortest path between reward locations.

For the simulations, we have defined a circular simulation area with radius being 1 m, and moved our virtual rat within that, in order to be consistent in term of size. Path algorithm explaining the movement of a foraging rat is derived from (Hasselmo et al., 2007) and can be summarized by the following equations:

$$\begin{aligned}\Delta x(t) &= S(1 - m)p_x + m\Delta x(t - 1) \\ \Delta y(t) &= S(1 - m)p_y + m\Delta y(t - 1)\end{aligned}\quad (4)$$

where $S = 5$, $m = 0.9$, and $p_x, p_y \sim \mathcal{N}(0, 1)$. This way, rat's motion heavily depends on its momentum, i.e., it cannot change its direction drastically. To ensure that rat stays within the boundaries of the simulation area, we use the following formulas

$$\begin{aligned}\Delta x_r(t) &= -\Delta x(t) \\ \Delta y_r(t) &= -\Delta y(t)\end{aligned}\quad (5)$$

whenever rat initiates a motion towards out of the boundaries, and we basically reflect that motion. In Figure 2(a) the locations at which the grid cell spikes are superimposed on the experimental trajectory are shown in red. Each red dot corresponds to one spike. Figure 2(b) and 2(d) shows the grid cell spikes on the simulated trajectory and place cell spikes on experimental trajectory, respectively.

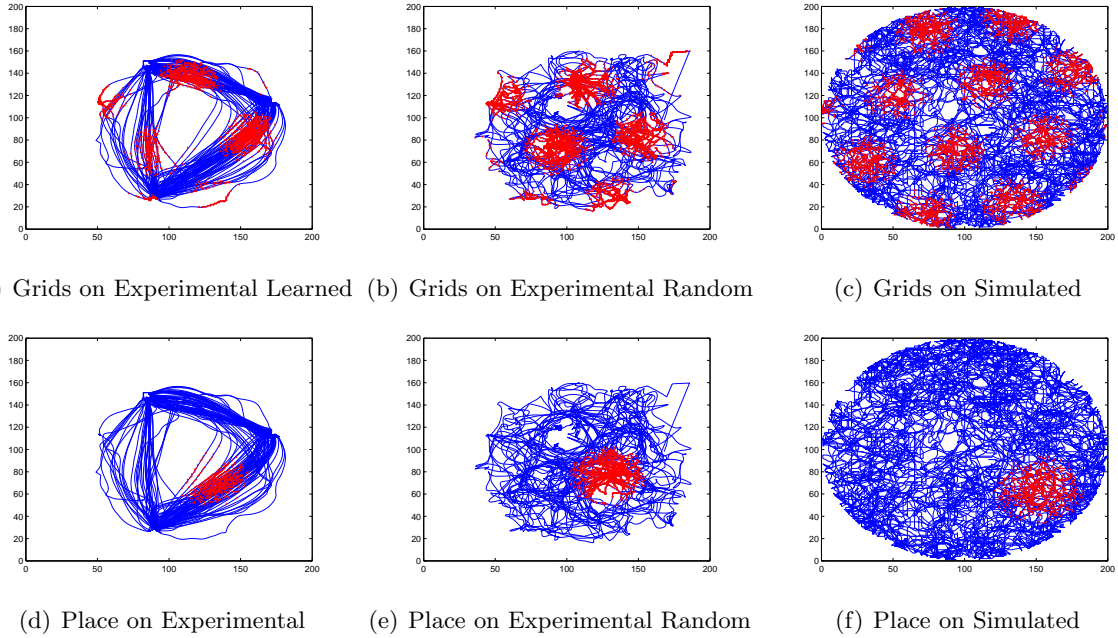


Figure 2: Grid and Place Cell Spikes Superimposed on Experimental and Simulated Trajectories

In order to retrieve the active cells at a given time, we first initialize a $t \times n$ `RetrieveActive` matrix with 0s, where t is the total simulation time and n is the number of grid/place cells. Then, the location of the rat is acquired at a given time, and if that location is within a place/grid field, the corresponding entry in the `RetrieveActive` matrix is changed into 1. Using this matrix, average firing rate for grid and place cells have been plotted for simulated path, and the results are shown in Figure 3(a) and 3(b), respectively. In addition, the average firing rate for grid and place cells for experimental path are shown in Figure 3(c) and 3(d), respectively.

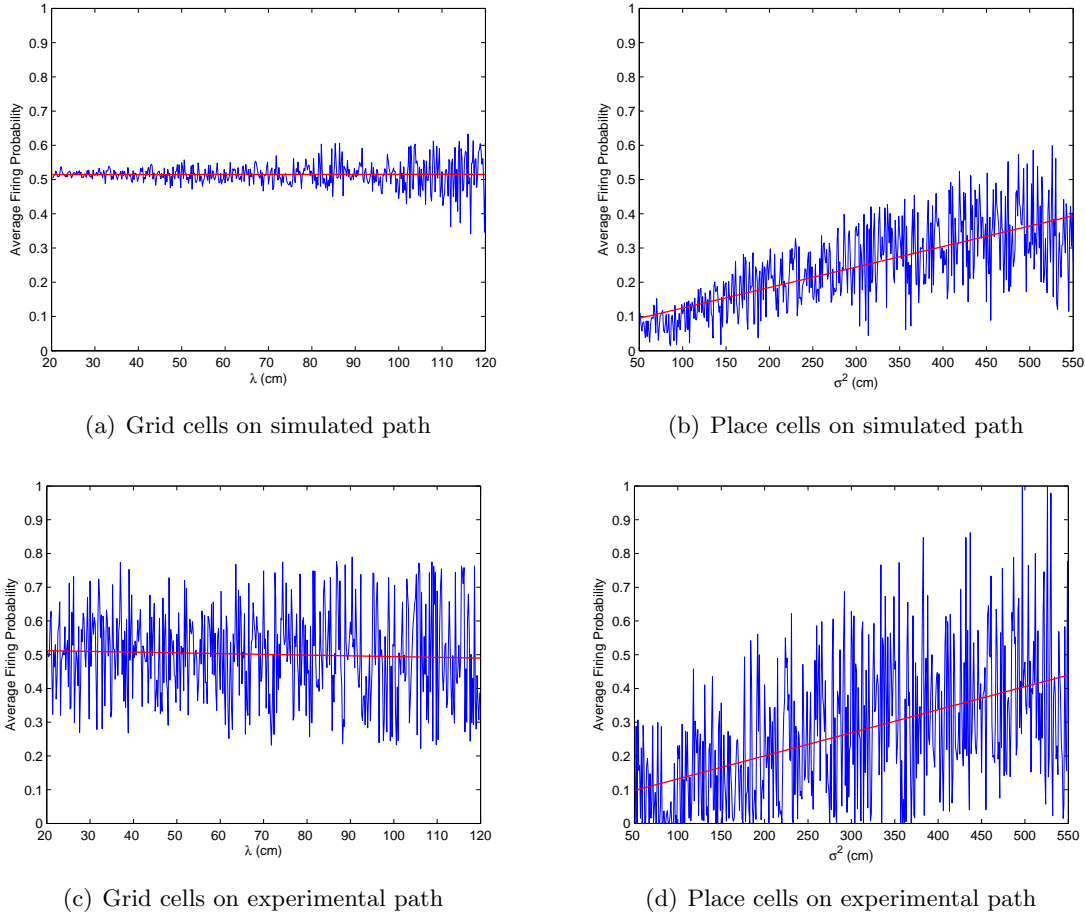


Figure 3: Average Firing Probability versus Field Radius for Simulated and Experimental Paths

Here, we assume that the rat is considerably slow. Thus, when we sample from two points consecutively, $(x(t), y(t))$ and $(x(t + \delta), y(t + \delta))$ are almost equal to each other, i.e., $\delta \approx 0$.

2.3 Learning Neural Connectivity Over Navigational Path

To acquire some knowledge about the synaptic connectivity of the neurons, we try to obtain the weight matrix between grid and place cells. For that purpose, we started with unsupervised Hebbian rule where the matrix entries w_{ij} s are updated as follows

$$w_{ij}(t) = w_{ij}(t - 1) + \alpha x_i(s(t))x_j(s(t)) \quad (6)$$

Here, $s(t)$ is the stimuli at time t , α is the learning rate, x_i is the pre-synaptic neuron and x_j is the post-synaptic neuron. w_{ij} s corresponds to synapses, and as a result, when two cells 'fire together they wire together'. As expressed in the Equation 6, when both neurons fire with stimuli $s(t)$, we update both w_{ij} and w_{ji} , regardless of which neuron fires first. Thus, the resulting weight matrices are symmetric. We start with initializing the matrix with zeros and update the entries at each location on the path. We use the firing probabilities of place and grid cells as described in Equations 1 and 3, for x_i and x_j .

However, one problem with unsupervised Hebbian rule is that the entries can grow without bounds. To overcome this, we decided to switch to the Hebbian rule with decay and modified our

update equation by adding a decay element as follows

$$w_{ij}(t) = \begin{cases} w_{ij}(t-1) + \alpha_{ij}x_i(s(t))x_j(s(t)) & \text{if } x_i(s(t)) \cdot x_j(s(t)) > 0 \\ w_{ij}(t-1) - \gamma_{ij}x_i(s(t)) & \text{if } x_j(s(t)) = 0, x_i(s(t)) \geq 0 \end{cases} \quad (7)$$

where $\gamma_{ij} = \gamma$ is the decay rate. Here, α_{ij} depends on i and j in order to ensure modularity. Because, we found out that when α is homogeneous across all i, j pairs, we cannot achieve modularity. For that purpose, we have defined $\alpha_{ij} = 0.3$ when $i, j \in [1, 100]$ or $[101, 200]$ or $[201, 300]$ or $[301, 400]$ or $[401, 500]$ and $\alpha_{ij} = 0.05$ otherwise. In Equation 7, we should not decrease w_{ij} s if neither $x_i(s(t))$ nor $x_j(s(t))$ is nonzero; otherwise, associations will be lost if stimuli is not occasionally present. When using this equation, we should take the negative entries to zero, since w_{ij} s cannot be negative by definition.

3 Results

3.1 1D Analysis

Here, we are trying to find out the relationship between the periods of two grid cells in order to maximize the cross-correlation between their firing fields. We assume the cells span 1D space.

In 1D, the cross-correlation formula of two cells can be represented as

$$\int_0^R (1 + \cos(\frac{2\pi}{\lambda_1}x + \phi_1))(1 + \cos(\frac{2\pi}{\lambda_2}x + \phi_2))dx \quad (8)$$

where R is the length of the simulation area, λ_1 and λ_2 are the periods, ϕ_1 and ϕ_2 are the phases of the first and the second cell, respectively. If we assume the phases are equal to 0 and analytically solve the equation, we get

$$\begin{aligned} \int_0^R (1 + \cos(\frac{2\pi}{\lambda_1}x + \phi_1))(1 + \cos(\frac{2\pi}{\lambda_2}x + \phi_2))dx &= \int_0^R (1 + \cos(\frac{2\pi x}{\lambda_1}) + \cos(\frac{2\pi x}{\lambda_2}) + \cos(\frac{2\pi x}{\lambda_1})\cos(\frac{2\pi x}{\lambda_2}))dx \\ &= R + \frac{\lambda_1}{2\pi} \sin \frac{2\pi R}{\lambda_1} + \frac{\lambda_2}{2\pi} \sin \frac{2\pi R}{\lambda_2} + \frac{\lambda_1 \lambda_2}{4\pi(\lambda_1 - \lambda_2)} \sin \frac{2\pi R(\lambda_1 - \lambda_2)}{\lambda_1 \lambda_2} + \frac{\lambda_1 \lambda_2}{4\pi(\lambda_1 + \lambda_2)} \sin \frac{2\pi R(\lambda_1 + \lambda_2)}{\lambda_1 \lambda_2} \end{aligned} \quad (9)$$

The fourth term in (9) is equal to

$$\frac{R}{2} \operatorname{sinc}(\frac{2\pi R(\lambda_1 - \lambda_2)}{\lambda_1 \lambda_2})$$

which is maximized as $(\lambda_1 - \lambda_2) \rightarrow 0$. The fifth term, on the other hand, is equal to

$$\frac{R}{2} \operatorname{sinc}(\frac{2\pi R(\lambda_1 + \lambda_2)}{\lambda_1 \lambda_2})$$

which is maximized as λ_1 and λ_2 gets larger. Accordingly, second and third terms can also be rewritten as

$$R \operatorname{sinc}(\frac{2\pi x}{\lambda_1})$$

and

$$R \operatorname{sinc}(\frac{2\pi x}{\lambda_2}),$$

which are also maximized as λ_1 and λ_2 gets larger. In short, we can say that the integral is maximized when $\lambda_1 = \lambda_2$ and they are both large.

If we rewrite (9) with *sinc* terms, we get

$$= R(1 + \text{sinc}\left(\frac{2\pi x}{\lambda_1}\right) + \text{sinc}\left(\frac{2\pi x}{\lambda_2}\right) + \frac{1}{2} \text{sinc}\left(\frac{2\pi R(\lambda_1 - \lambda_2)}{\lambda_1 \lambda_2}\right) + \frac{1}{2} \text{sinc}\left(\frac{2\pi R(\lambda_1 + \lambda_2)}{\lambda_1 \lambda_2}\right)) \quad (10)$$

In order to compute the integral, we assumed that $R = 200\text{cm}$ and we have used 3 reference periods which are 40 cm, 60 cm and 80 cm. The resulting value of the normalized integral versus the second λ value is shown in Figures 4(a), 4(b) and 4(c) for all 3 reference λ values.

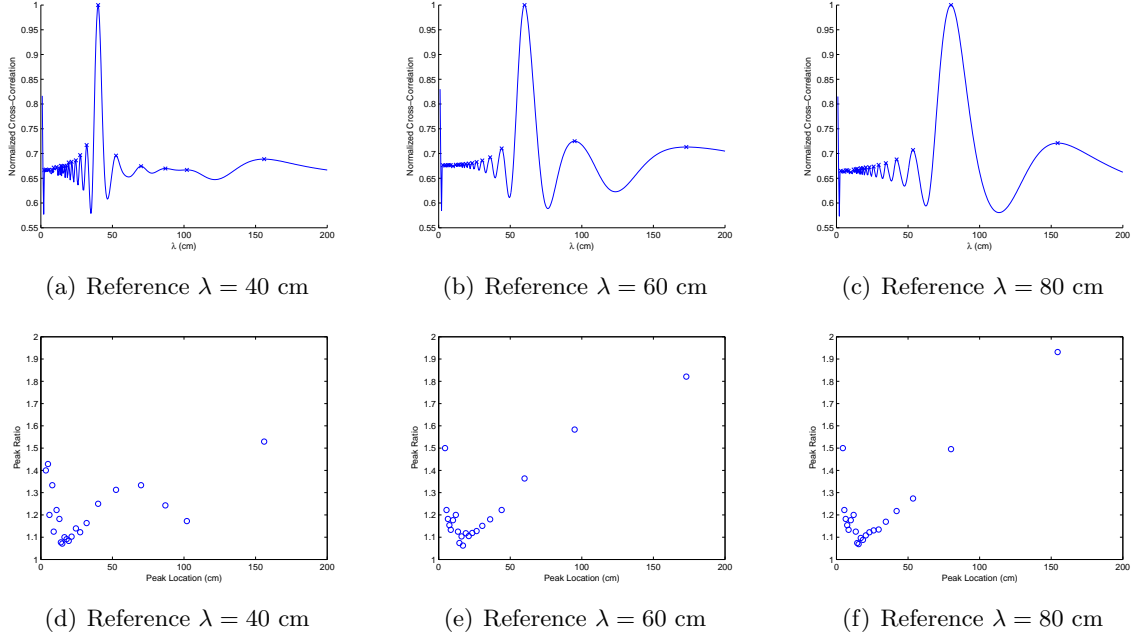


Figure 4: Top row: Normalized Cross-correlation in 1D versus λ for 3 Reference Periods. Bottom row: Ratio of the two consecutive peaks versus peak locations.

We also investigate the ratio of the two consecutive peaks in Figures 4(d), 4(e) and 4(f). The average peak ratio is 1.2128 in Figure 4(d), 1.2249 in Figure 4(e) and 1.2192 in Figure 4(f). The findings are compatible with Moser's paper. (ref)

3.2 2D Analysis

Here we did the same analysis we did 1D.

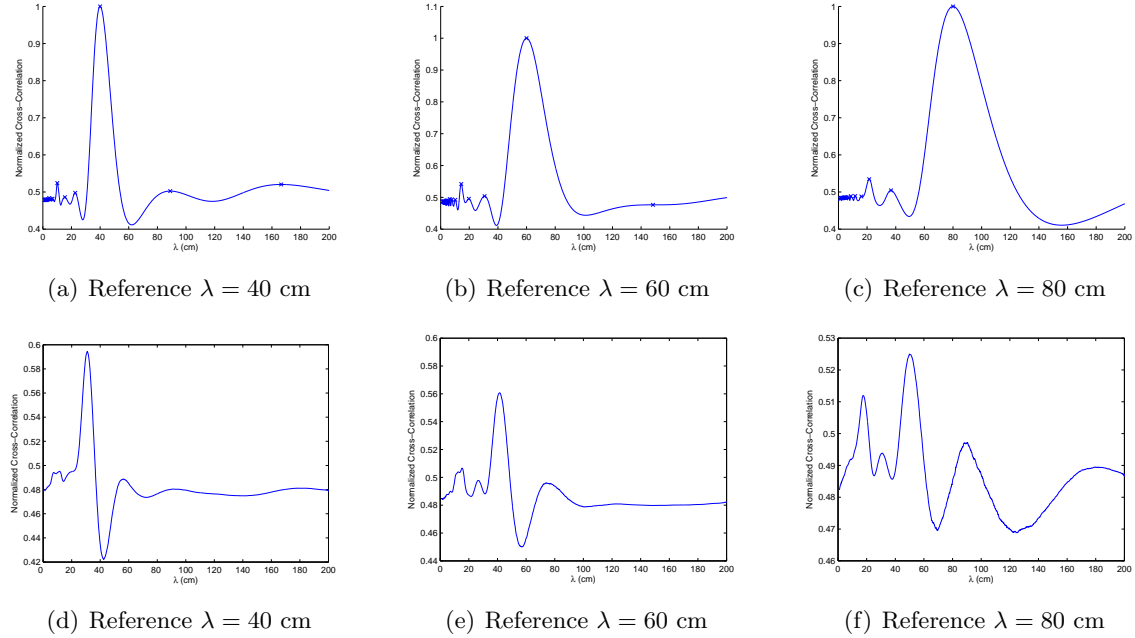


Figure 5: Normalized Cross-correlation in 2D versus λ for 3 reference periods. Top row: Phases are assumed to be equal. Bottom row: Results averaged over random phase

The average peak ratio is 2.0189 in Figure 5(d), 1.6965 in Figure 5(e) and 1.7895 in Figure 5(f).

In addition, we wanted to see the effect of the period and orientation together. For that purpose, we plotted a 3D graph that shows period, orientation and cross-correlation altogether, and that graph is shown in Figure 6.

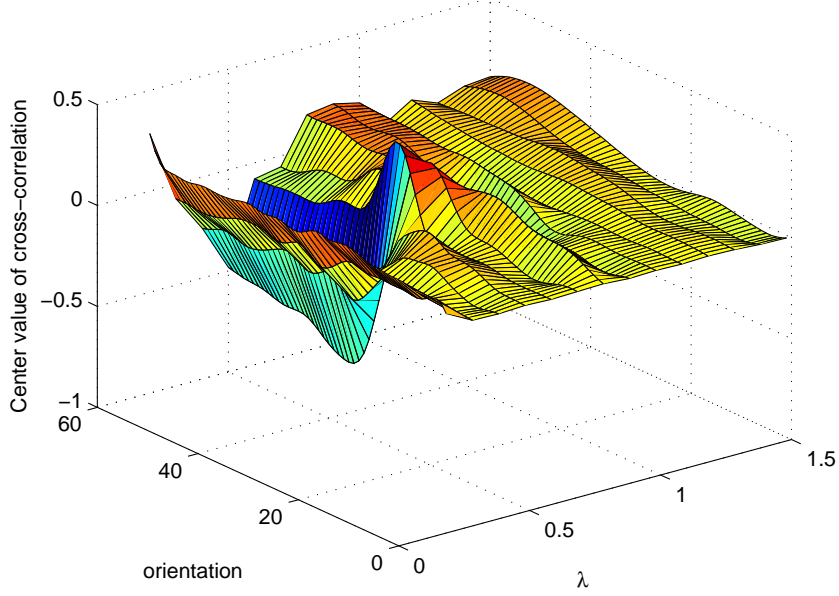


Figure 6: Central value of the cross-correlation versus λ and orientation for an $4m \times 4m$ simulation area

The new 3D figure is shown in Figure

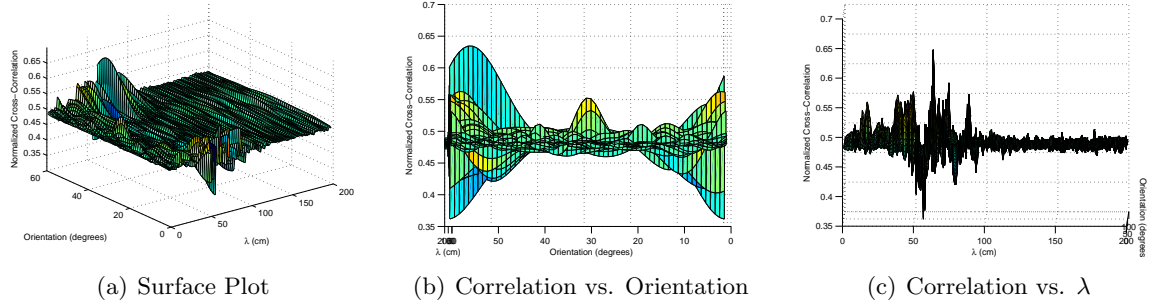


Figure 7: Normalized Cross-correlation in 2D versus λ and orientation for an $2m \times 2m$ simulation area. Reference $\lambda = 60$ cm and the reference orientation = 0 degrees.

3.3 Main Part

Starting with a homogeneous, smooth distribution of firing field gradients of place and grid cells, we study the structure of the weight matrix when actual paths recorded from rodents are followed. Two conditions were considered: random foraging and learning of paths between specific rewarded locations. We observed significant differences in the resulting weight matrices. The weight matrix corresponding to foraging shows a smooth connectivity pattern throughout the synaptic population. On the other hand, the weight matrix of the path with reward locations shows a clear pattern consisting of sub-modules organized along the dorso-ventral axis in the grid-grid connectivity region. This result suggests that grid cells synaptically group themselves in modules on a learned path. However, this modularity does not appear in place-place or grid-place connections. These

results are compatible with, and may partially explain, the electrophysiological results obtained experimentally.

Using the resulting weight matrices as a feedback, we then update the periods of the grid cells in both scenarios. We hope to see a modular formation in the periods of the cells when the rat follows a learned path. Overall, our plasticity-based framework is a novel computational model that suggests a mechanism for the formation of dorso-ventral modules in grid cells.

We have applied Equation 7 with $\alpha = 0.3$ and $\gamma = 0.6$ on the simulated path of a foraging rat and experimental path with reward locations. The resulting weight matrices are shown on Figure 8 with the corresponding paths.

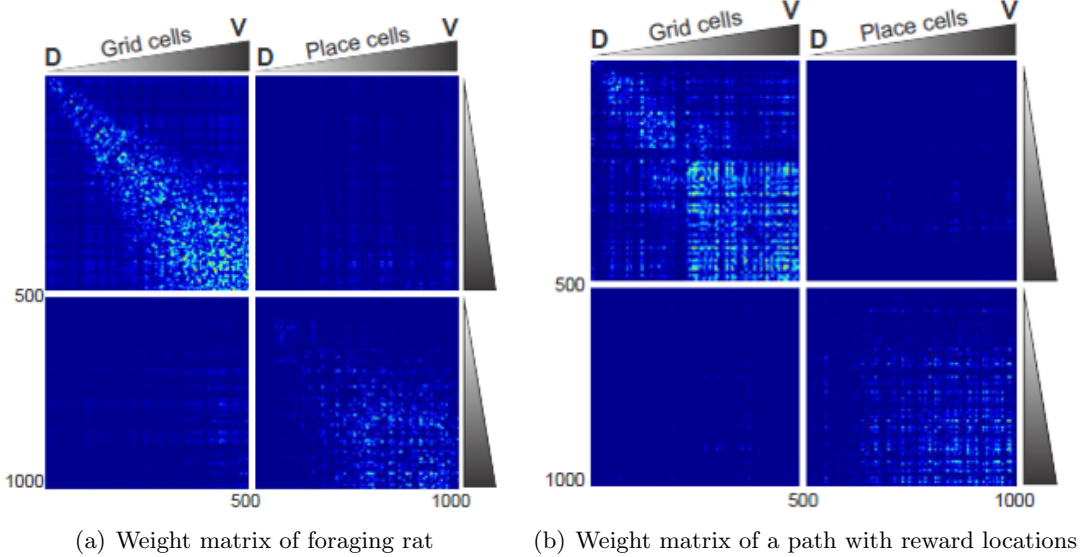


Figure 8: Weight matrices based on experimental data, showing grid-grid, grid-place, place-grid and place-place connectivities in the upper left, upper right, lower left and lower right regions, respectively.

In the next step, we have used the weight matrix as a feedback, in order to update the firing probabilities of the cells. In other words, for a given cell i , we can find a cell j such that w_{ij} is the highest in row i . Then, we can increase the conditional firing probability of cell j , $P(j | i)$, given that cell i fires. This may correspond to increasing the radius of cell j 's tuning curve when cell i fires, or even merging their tuning curves. After that, we can recompute the weight matrix and continue this process until the system converges to steady state. The flowchart of the proposed algorithm is shown in Figure 9.

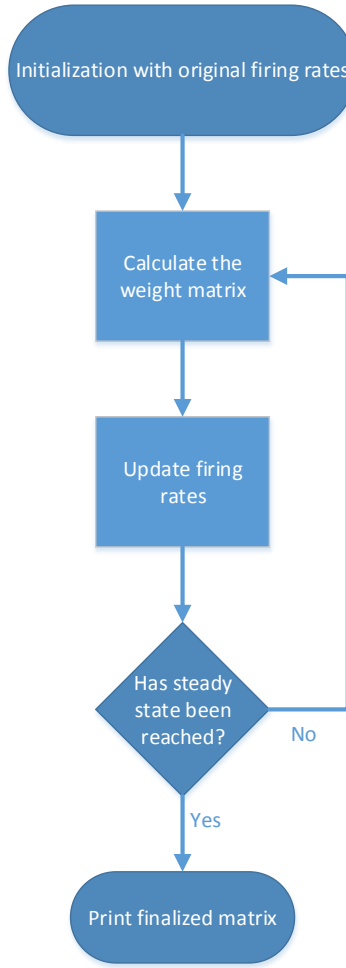


Figure 9: Proposed algorithm that updates the firing rate according to weight matrix entries

We have implemented this algorithm as follows: First, we have started with the original values of λ s that are continuously increasing and computed our first weight matrix. Then, we have updated our λ values such that

$$\lambda_j(t) = \alpha\lambda_j(t-1) + (1-\alpha)\frac{\sum_{i \in N_j} W_{ij}\lambda_i}{\sum_{i \in N_j} W_{ij}} \quad (11)$$

where α is a constant that determines how much the updated value will depend on the previous value, W_{ij} is the weight matrix entry between cell i and cell j , and N_j is the neighborhood of cell j that consists of the cells that are strongly connected to that cell. We have continued to calculate the weight matrices and updating λ values until the steady state has been reached, according to

$$\lambda(t) - \lambda(t-1) \stackrel{?}{<} \epsilon \quad (12)$$

One can think of this formula as a basic update rule to change the tuning curves. However, later, we might consider moving on with a more detailed model that also considers the locations of the centers of grid fields and updates the tuning curve accordingly.

In addition, we wanted to see the effects of the initial conditions of λ . For that purpose, we considered three conditions: continuously increasing λ s, modular λ s and random λ s. The results of the continuously increasing and random λ s were similar, so we included the resulting weight matrices of continuously increasing λ s and modular λ s in Figure 10. The resulting λ values of the corresponding cases are also shown in Figure 19.

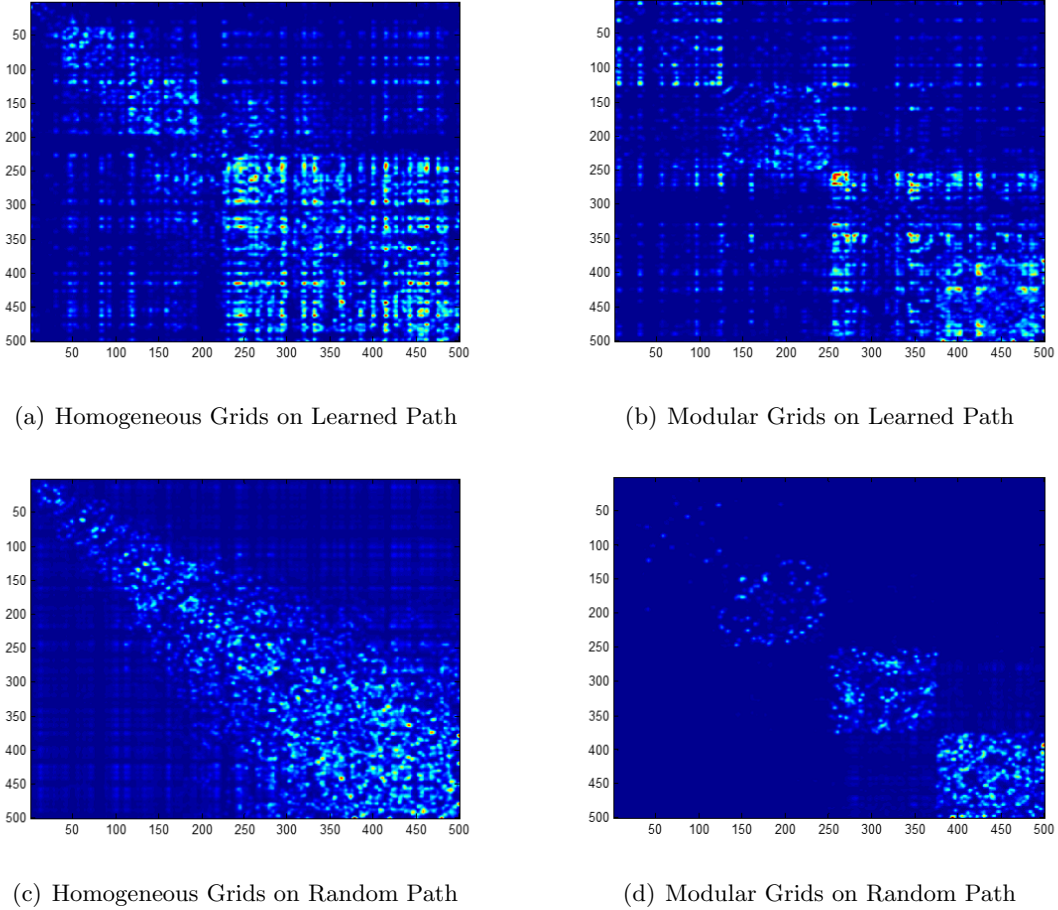


Figure 10: Formation of Weight Matrix with Different Initial Conditions and Paths

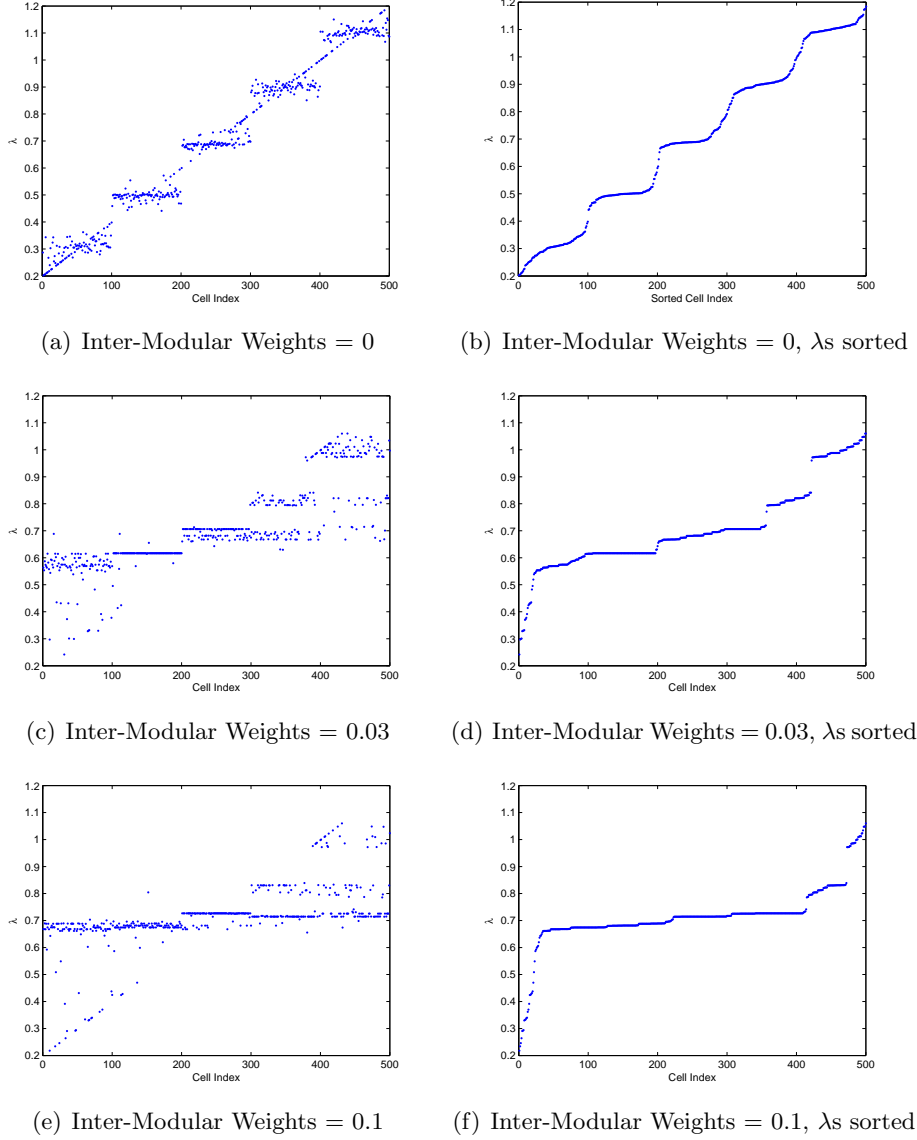


Figure 11: Disappearance of the modular structure as the inter-modular weights increase from 0 to 0.1, when intra-modular weights are 0.3

Here, we see that the modules form when the contribution of the λ_s of the cells outside a region of a specific cell is 0. This modular structure disappears as we increase the inter-modular contribution up to 0.1. Here we start with homogeneous λ_s initially.

4 Appendix

4.1 Effect of Velocity

We also wanted to observe the effect of change in the velocity of the animal on the formation of the weight matrix. For that purpose, we sampled the path less frequently to increase the speed and more frequently to decrease it. The resulting weight matrices are shown in Figure 12.

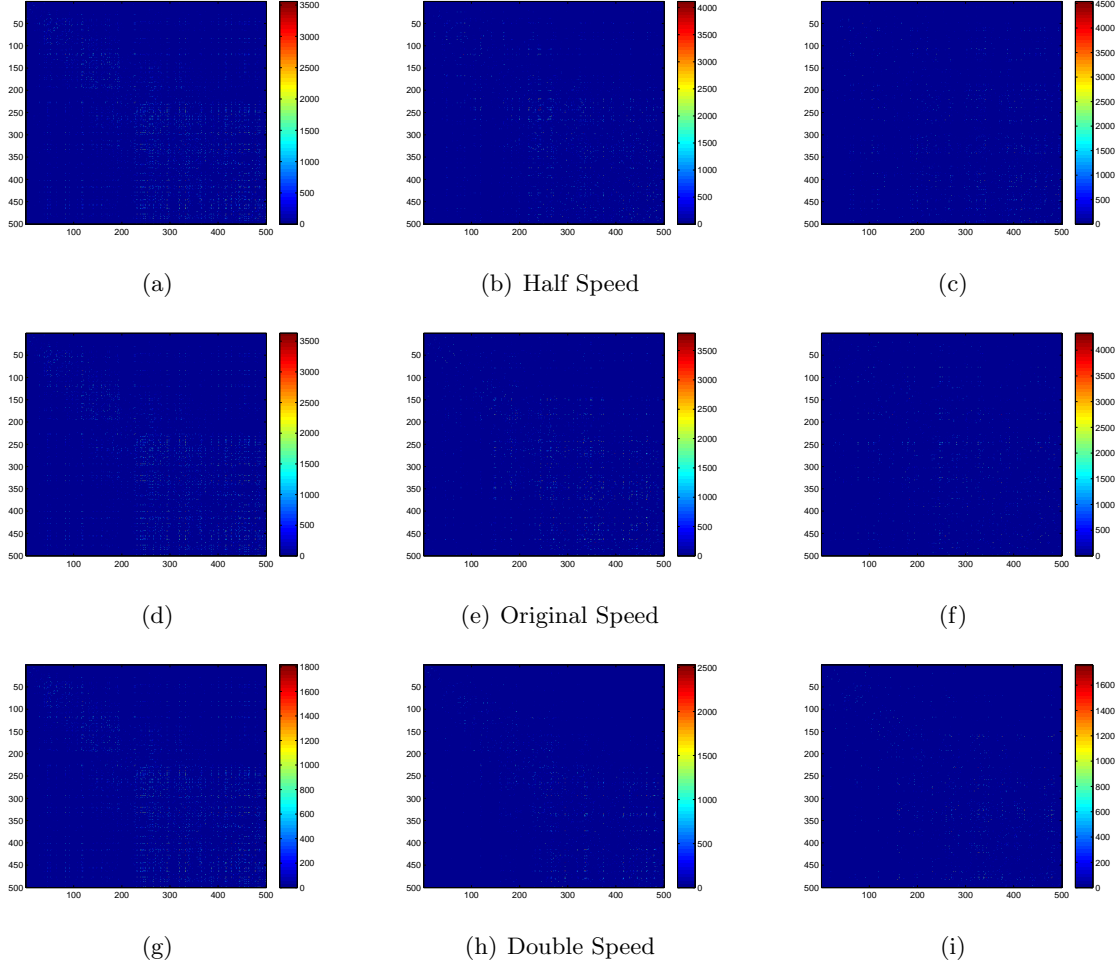


Figure 12: Effect of velocity on the formation of the weight matrix

4.2 Sparseness and Average Weight

Sparseness and average weight graphs are shown in Figure 13(a) and 13(b), respectively. Colors of the bars are in accordance to the regions in the color map (dorsal-dorsal, dorsal-ventral, ventral-ventral) in Figure 13(c). Transparent colored bars belong to the data of learned path and the opaque bars belong to the random path.

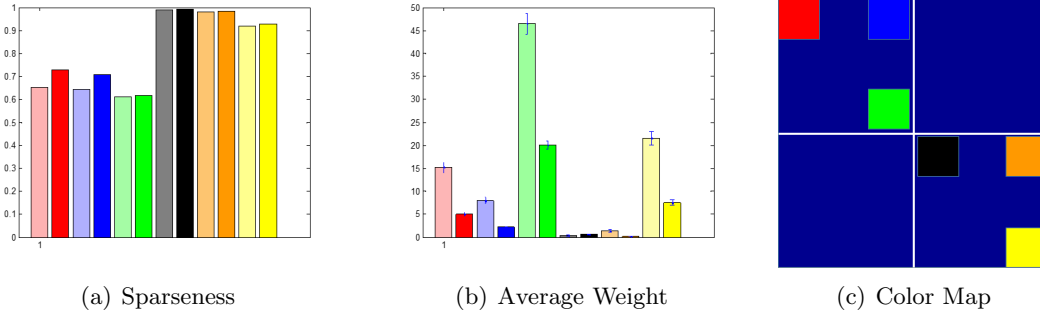


Figure 13: Sparseness and Average Weight Bar Charts with the Corresponding Color Map

4.3 June 22 Omitted

The weight matrices obtained by using Equations 6 and 7 are shown in Figures 14(a) and 14(b), respectively.

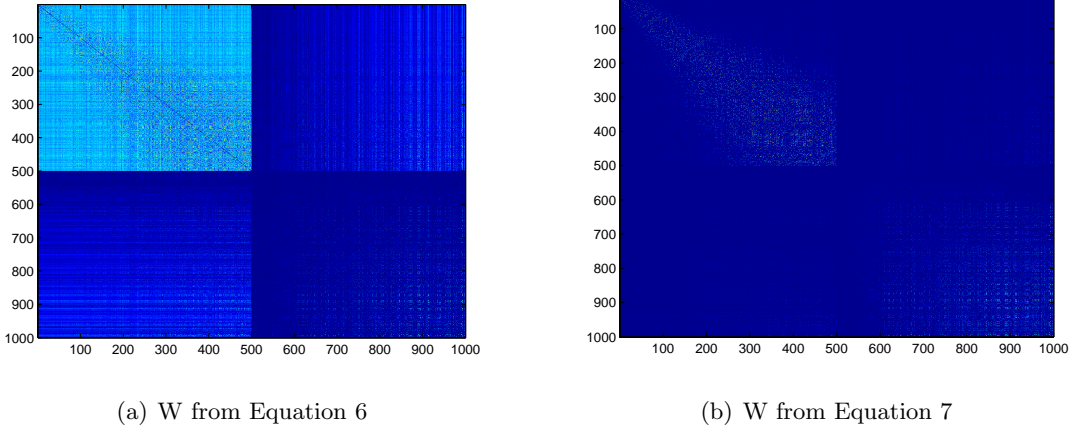


Figure 14: Weight matrices showing grid-grid, grid-place, place-grid and place-place connectivities in the upper left, upper right, lower left and lower right regions, respectively. In each region, left to right and upper to lower transitions correspond to dorsal to ventral transitions.

We have plotted Figure ?? again with more λ values, and in return better resolution. In addition to the previous figure, here we take the average of 9 central values in the graph instead of taking only the center point. The resulting graph is shown in Figure 4.3.

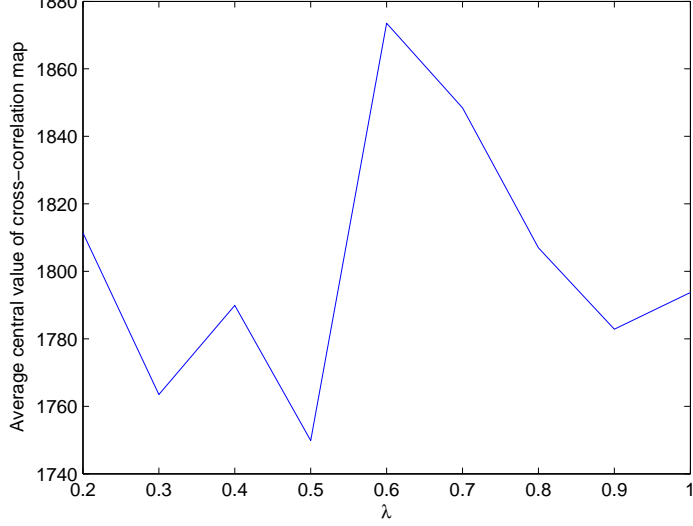


Figure 15: Average of central values vs. λ

Finally, we wanted to see the effect of the path on the cross-correlation. For that purpose, we multiplied the two rate maps of two different cells generated by (3) and superimposed the product on the learned path and on the random path. We choose the index of the reference cell as 250,

which corresponds to a period of 0.6 meters, and the period of the second cell varies between 0.2 meters to 1.2 meters in accordance with the cell index. The resulting graph is shown in Figure 4.3, but it needs to be averaged over random phase and orientation.

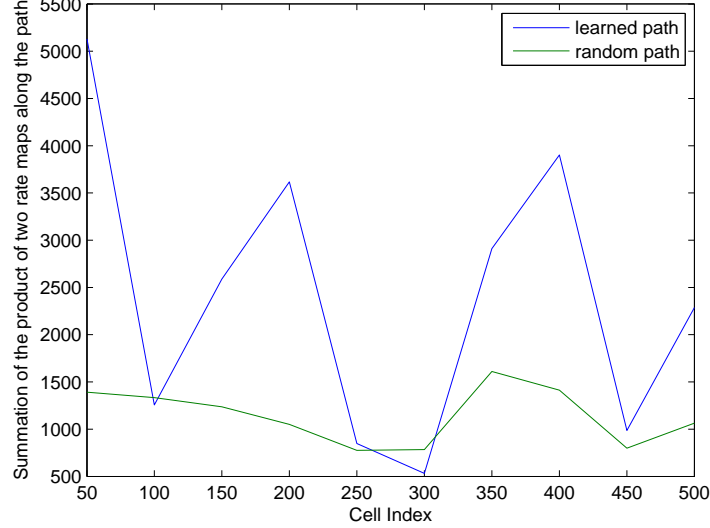


Figure 16: Product of two rate maps superimposed on the learned and the random path vs. cell index

After the final λ values are calculated, we have clustered them into several modules. The resulting graphs for the learned path and the random path are shown in Figure 17.

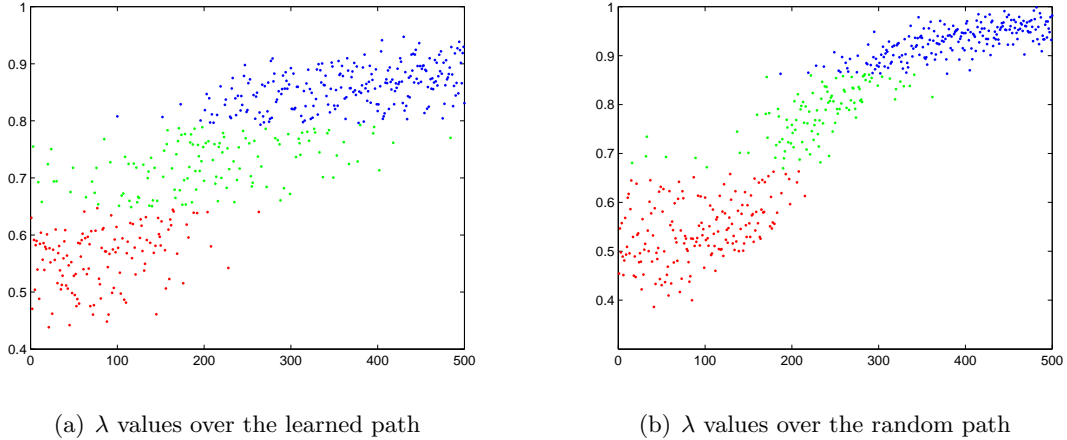
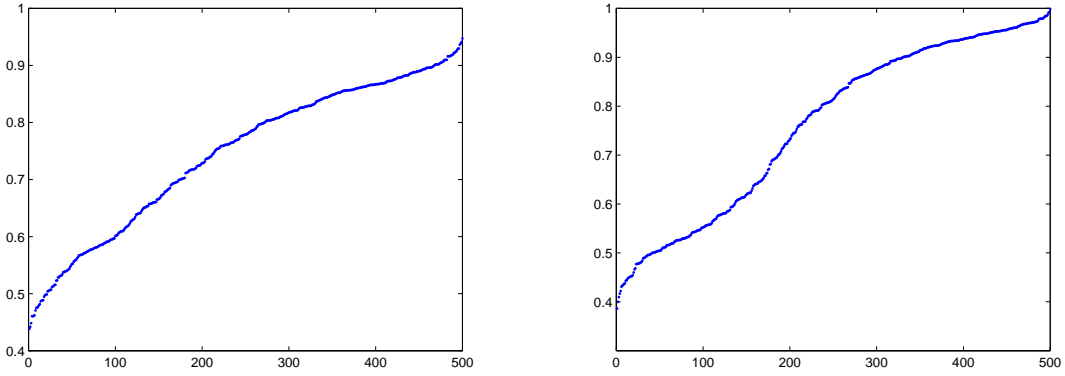


Figure 17: Updated and clustered λ values over learned and random paths

If we calculate the mean values of the clusters in both paths, we see that $\lambda_{mean} = [0.5431, 0.7818, 0.9304]$ for the random path and $\lambda_{mean} = [0.5612, 0.7242, 0.8595]$ for the learned path.

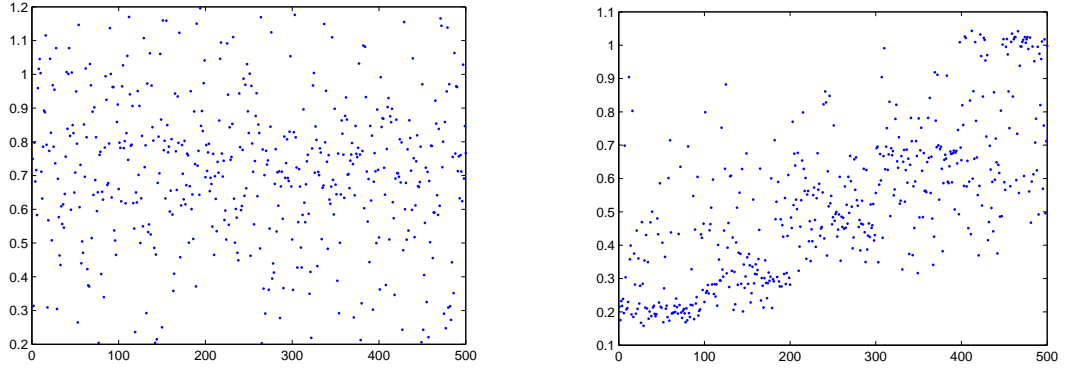
The sorted λ values of the same scenarios are also shown in Figure 18.



(a) Sorted λ values over the learned path

(b) Sorted λ values over the random path

Figure 18: Updated, clustered and sorted λ values over learned and random paths



(a) Homogeneous λ values over the random path

(b) Modular λ values over the learned path

Figure 19: Updated λ values over learned path when started with homogeneous and modular λ

Here, we vary the simulation area and use normalized 2D cross-correlation function for our analysis. Our first simulation area is $3m \times 3m$ and we use three reference λ values for our analysis: 0.3m, 0.6m and 0.9m. We vary the second cell's period from 0.2m to 1.5m. Normalized cross-correlation graphs are shown in Figure 20, and the change of the central value of the cross-correlation w.r.t period, for different reference periods are shown in Figure 23.

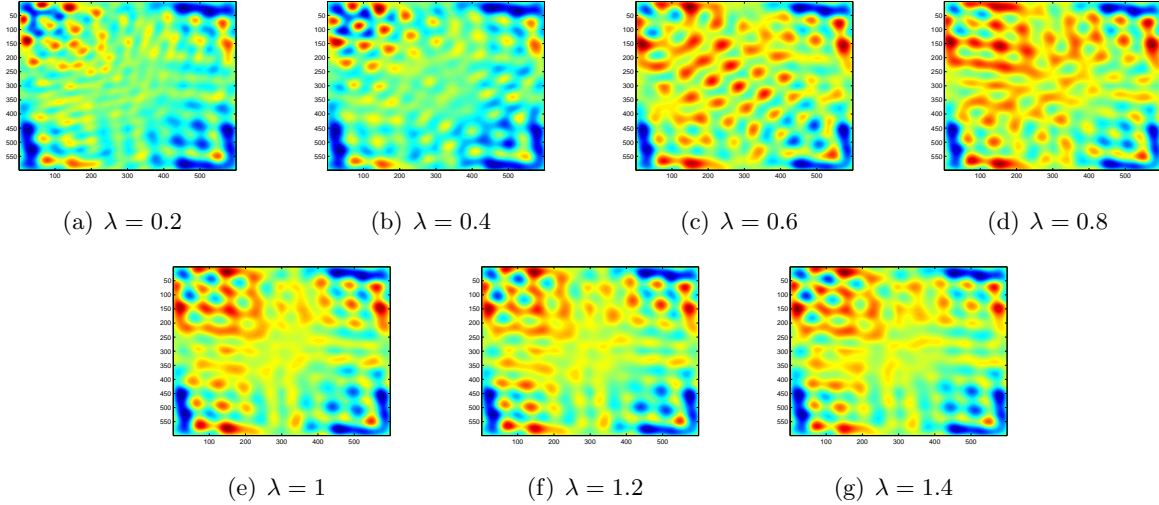


Figure 20: Normalized cross-correlation of grid cell firings with different periods averaged over 500 trials ($\lambda = 0.6$ for the reference cell and the simulation area is $3m \times 3m$)

Here, we have investigated the effect of the periods of two cells on the cross-correlation of their firing fields. For that purpose, we have set the period of the reference cell as 0.6 meters and varied the period of the second cell from 0.2 meters to 1 meter. We have averaged the results over random phase and orientation. Figure 21 shows the resulting cross-correlation maps for different periods.

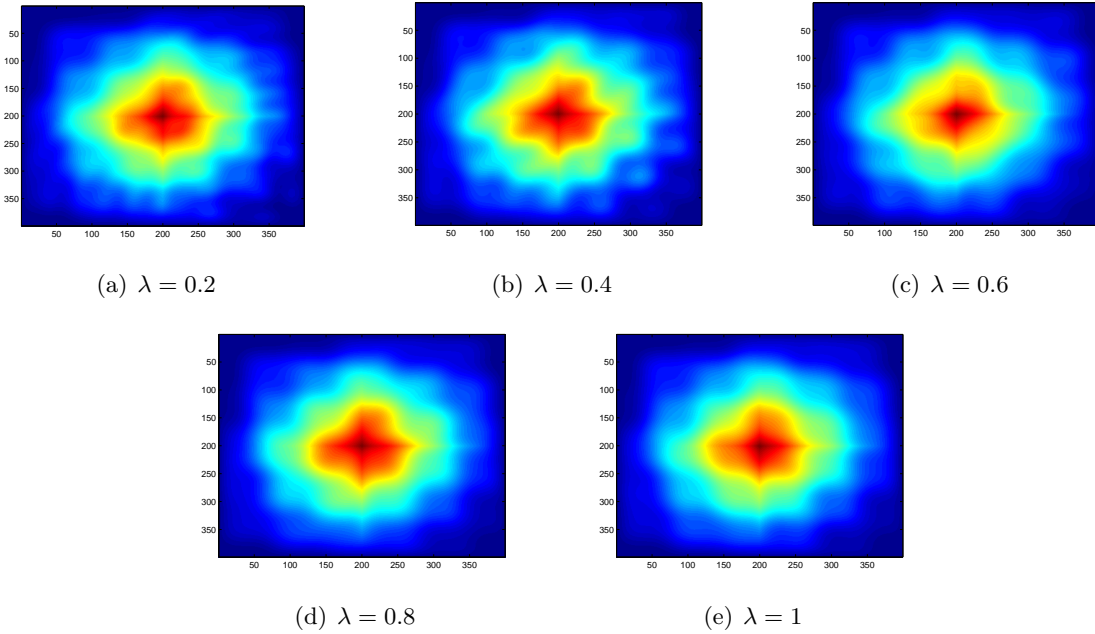


Figure 21: Cross-correlation of grid cell firings with different periods averaged over 500 trials ($\lambda = 0.6$ for the reference cell)

We have also investigated the effect of the orientations of the two cells on cross-correlation. For that purpose, we have set the orientation of the reference cell to $\pi/6$ and varied the orientation of the second cell from $\pi/18$ to $\pi/3$. We have averaged the results over random phase and periods.

Figure 22(a) shows the change in the center value of the cross-correlation map w.r.t λ and Figure 22(b) shows the change in the center value of the cross-correlation map w.r.t orientation.

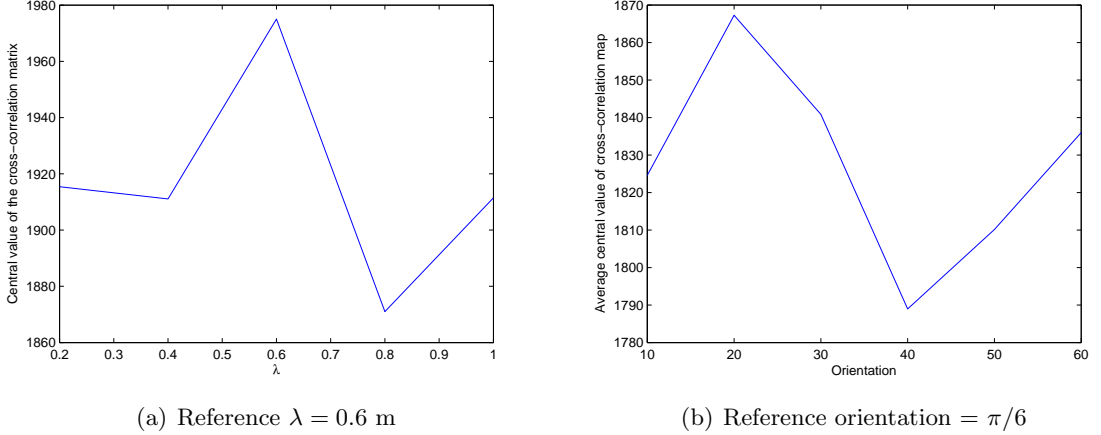


Figure 22: Cross-correlation versus λ and orientation for an $3m \times 3m$ simulation area

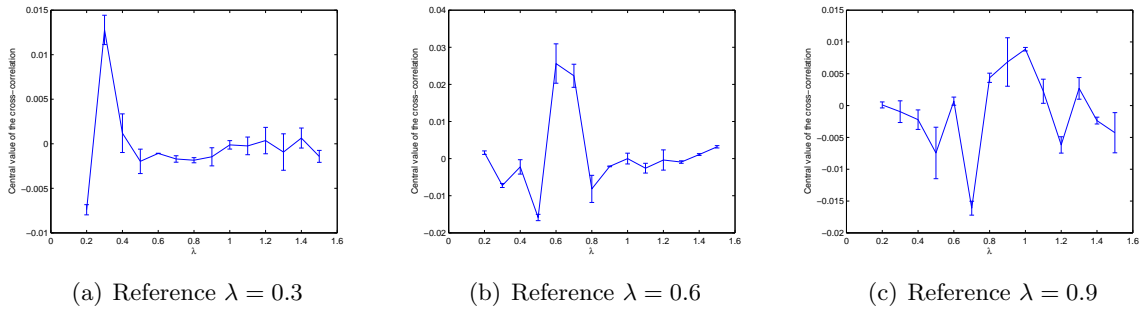


Figure 23: Central value of the cross-correlation versus λ for different reference λ values for an $3m \times 3m$ simulation area

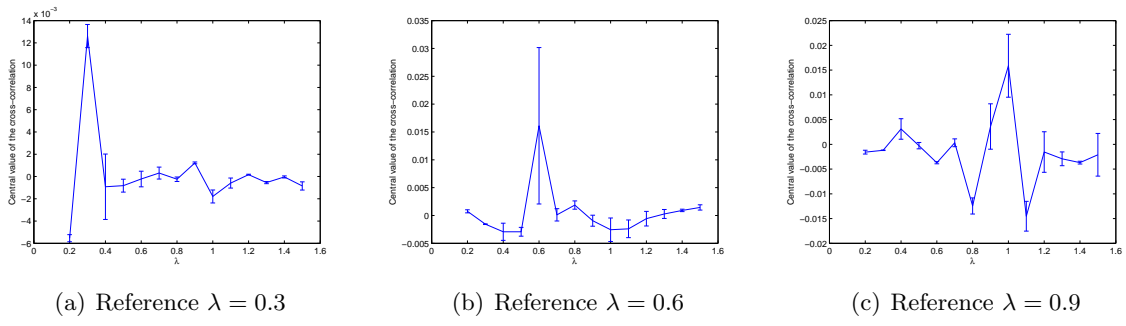


Figure 24: Central value of the cross-correlation versus λ for different reference λ values for an $4m \times 4m$ simulation area

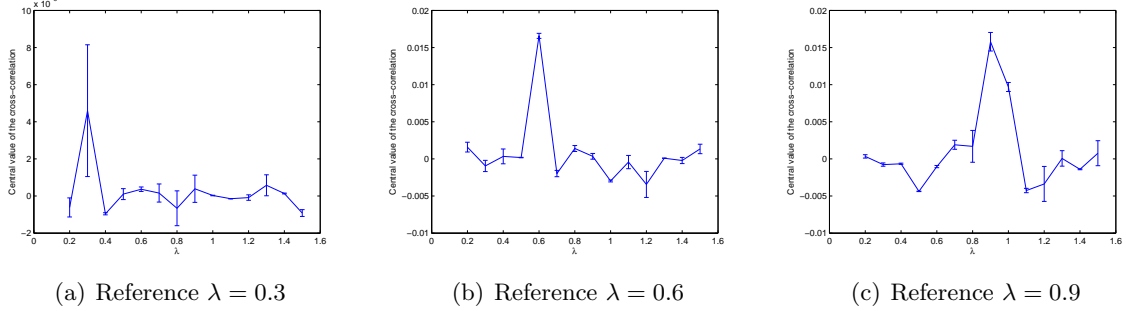


Figure 25: Central value of the cross-correlation versus λ for different reference λ values for an $5m \times 5m$ simulation area

4.4 Codebook Simulation

We have created a modular grid simulation such that the values of λ are taken from a normal distribution and the mean of the distribution increases by x times between modules ($x=1:0.4:3$), across the dorso-ventral axis. For the simulation, we have considered the following parameters:

Simulation time = 1000 units

Number of Modules = 5

Number of Cells per Module = 50

Number of Paths = 10

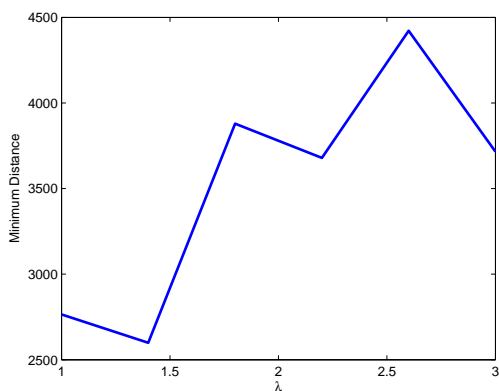
Number of Codes = 5

Number of Reward Locations = 3:10

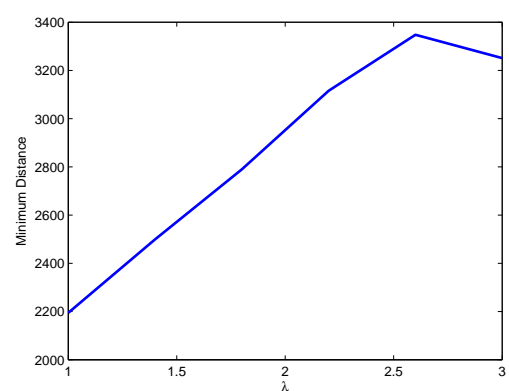
At each λ value, we have run the simulation for several paths and obtained the resulting weight matrices. The i,j values that satisfies

$$\arg \min_{i,j} \|W_i - W_j\| \quad (13)$$

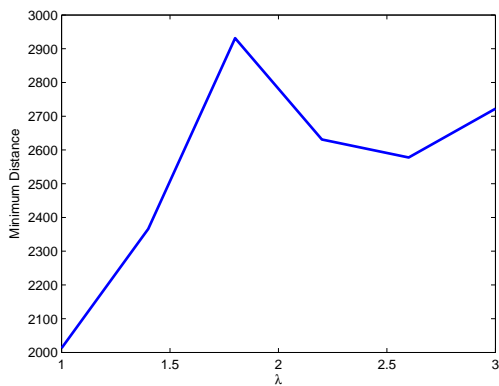
where $\|x\|$ corresponds to l-2 norm of vector x , give us the minimum distance of the codebook corresponding to that λ value. We would like to find the optimum λ values to maximize the minimum distance, since larger minimum distance implies higher noise resilience and may biologically mean that it is easier to distinguish between different paths. However, the optimum λ values are different for different number of reward locations. Some cases are given below.



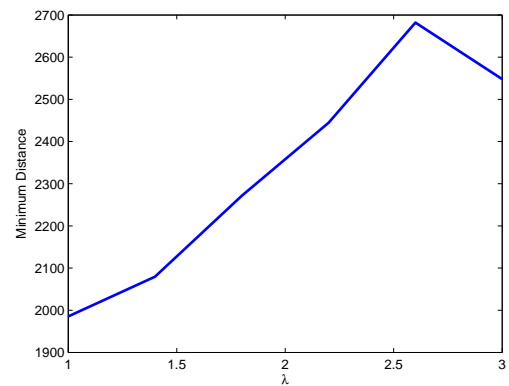
(a) Reward Locations = 3



(b) Reward Locations = 4



(c) Reward Locations = 5



(d) Reward Locations = 6

Figure 26: Minimum distance versus λ for various number of reward locations

5 References

- Arleo A, Gerstner W (2000) Spatial cognition and neuro-mimetic navigation: a model of hippocampal place cell activity. *Biological Cybernetics* 83:287–299.
- Bostock E, Muller RU, Kubie JL (1991) Experience-dependent modifications of hippocampal place cell firing. *Hippocampus* 1:193–205.
- Brun VH, Solstad T, Kjelstrup KB, Fyhn M, Witter MP, Moser EI, Moser MB (2008) Progressive increase in grid scale from dorsal to ventral medial entorhinal cortex. *Hippocampus* 18:1200–1212.
- Burak Y, Fiete IR (2009) Accurate path integration in continuous attractor network models of grid cells. *PLoS computational biology* 5:e1000291.
- Burgess N, Barry C, O’Keefe J (2007) An oscillatory interference model of grid cell firing. *Hippocampus* 17:801–812.
- de Almeida L, Idiart M, Lisman JE (2009) The input–output transformation of the hippocampal granule cells: from grid cells to place fields. *The Journal of Neuroscience* 29:7504–7512.
- Fuhs MC, Touretzky DS (2006) A spin glass model of path integration in rat medial entorhinal cortex. *The Journal of Neuroscience* 26:4266–4276.
- Giocomo LM, Zilli EA, Fransén E, Hasselmo ME (2007) Temporal frequency of subthreshold oscillations scales with entorhinal grid cell field spacing. *Science* 315:1719–1722.
- Hafting T, Fyhn M, Molden S, Moser MB, Moser EI (2005) Microstructure of a spatial map in the entorhinal cortex. *Nature* 436:801–806.
- Hasselmo ME (2008) Grid cell mechanisms and function: contributions of entorhinal persistent spiking and phase resetting. *Hippocampus* 18:1213–1229.
- Hasselmo ME, Giocomo LM, Zilli EA (2007) Grid cell firing may arise from interference of theta frequency membrane potential oscillations in single neurons. *Hippocampus* 17:1252–1271.
- Lengyel M, Szatmary Z, Érdi P (2003) Dynamically detuned oscillations account for the coupled rate and temporal code of place cell firing. *Hippocampus* 13:700–714.
- Lever C, Wills T, Cacucci F, Burgess N, O’Keefe J (2002) Long-term plasticity in hippocampal place-cell representation of environmental geometry. *Nature* 416:90–94.
- Lyttle D, Gereke B, Lin KK, Fellous JM (2013) Spatial scale and place field stability in a grid-to-place cell model of the dorsoventral axis of the hippocampus. *Hippocampus* 23:729–744.
- McNaughton BL, Battaglia FP, Jensen O, Moser EI, Moser MB (2006) Path integration and the neural basis of the ‘cognitive map’. *Nature Reviews Neuroscience* 7:663–678.
- Moser EI, Kropff E, Moser MB (2008) Place cells, grid cells, and the brain’s spatial representation system. *Annu. Rev. Neurosci.* 31:69–89.
- Moser EI, Roudi Y, Witter MP, Kentros C, Bonhoeffer T, Moser MB (2014) Grid cells and cortical representation. *Nature Reviews Neuroscience* .

- O'Keefe J, Burgess N (1996) Geometric determinants of the place fields of hippocampal neurons. *Nature* 381:425–428.
- O'Keefe J, Nadel L (1978) *The hippocampus as a cognitive map* Clarendon Press Oxford.
- Savelli F, Knierim JJ (2010) Hebbian analysis of the transformation of medial entorhinal grid-cell inputs to hippocampal place fields. *Journal of neurophysiology* 103:3167–3183.
- Solstad T, Moser EI, Einevoll GT (2006) From grid cells to place cells: a mathematical model. *Hippocampus* 16:1026–1031.
- Tsodyks MV, Skaggs WE, Sejnowski TJ, McNaughton BL (1996) Population dynamics and theta rhythm phase precession of hippocampal place cell firing: a spiking neuron model. *Hippocampus* 6:271–280.
- Zilli EA, Hasselmo ME (2010) Coupled noisy spiking neurons as velocity-controlled oscillators in a model of grid cell spatial firing. *The Journal of neuroscience* 30:13850–13860.